RSC Advances

PAPER

View Article Online
View Journal | View Issue

Cite this: *RSC Adv.*, 2026, **16**, 27269

The role of 316 SS surface finishes in enhancing corrosion protection of conducting polyaniline coatings

Dat Minh Tran, [ab] Anh Thi Nhat Cao,[c] Ngo Thanh Binh, [d] Nhung Thi Nguyen, [ab] Casen Panaitescu, [e] Duong Ngo Kim Long, [ab] Nhi Ngoc Nguyen *[ab] and Nam Nguyen Dang [ab]

In the context of polymer-based anticorrosive coating, a surface finish strongly influences the adhesive and protective performance of polymer molecules on the metallic surface, particularly stainless steel (SS) as immersed in the simulated seawater. To achieve that, the ground 316 SS surface is treated by immersing it in a 1 M H_2SO_4 solution within 1 hour before polyaniline (PANi) is coated using a spin coating technique. This method generates effectively a thin, uniform layer on the SS substrate with controllable thickness. The study aims to evaluate the effects of acid-based surface treatment on the adhesion and protective performance of the PANi coating. In this study, surficial characterizations of the coated samples are analyzed using scanning electron microscopes (SEM), atomic force microscope (AFM), contact angle (CA), and attenuated total reflectance Fourier-transform infrared spectroscopy (ATR-FTIR). The results observed indicate that the PANi-coated samples reach a CA of 78 and 90° for the untreated and acid-treated surfaces, respectively. Electrochemical results show that the PANi coated/treated 316 SS surface in 3.5 wt.% NaCl solution has the highest pitting potential of 469 ± 20.2 $mV_{Ag/AgCl}$, with a protective efficiency up to ~94.7%. This advanced behavior is primarily attributed to the formation of a thin film on the 316 SS surface, including a passive oxide layer of SS as a buffer layer and a PANi layer, after treatment in the 1 M H_2SO_4 solution and spin coating respectively. Therefore, the work suggests an effective way to improve the adhesion and protective performance of the PANi coating on the 316 SS in various applications.

Received 26th February 2026
Accepted 30th April 2026

DOI: 10.1039/d6ra01684g

rsc.li/rsc-advances

1. Introduction

With the rapid development of modern industries, the demand for materials with advanced properties such as excellent mechanical strength, thermal stability, multi-functionality, and especially corrosion resistance, has been growing. These materials are developed to meet requirements of the performance, sustainability, and reliability of sectors, ranging from aerospace and automotive to electronics, energy, and biomedical engineering. Among them, 316 stainless steel (SS) is one of widely used versatile corrosion-resistant alloys in aggressive environments like seawater, chemical processing, medical implants, and food industry, due to its stable rich passive layer that provides excellent protection against localized corrosion.[1–5] These outstanding properties are attributed to its composition, particularly the presence of molybdenum (Mo), chromium (Cr), and nickel (Ni), which provides superior resistance to pitting and crevice corrosion, especially in chloride-rich environments. In which, Mo and Cr contributes to the enrichment and stabilization of the chromium-rich passive film ($Cr_{2-x}Fe_xO_3$), suppressing the initiation of metastable pits and reducing the susceptibility of the alloy to localized corrosion under chloride attack.[6–8] Simultaneously, alloying elements such as Mn and N further enhance the inherent corrosion resistance of 316 SS by promoting the formation of stable nitride phases, contributing to a dense mixed oxide layer and stabilizing the austenitic lattice.[9–12]

Despite its outstanding characteristics, when working continuously in highly corrosive environments, the gradual degradation of materials is unavoidable.[13–15] More specifically, after prolonged exposure in chloride-rich environments like seawater, the passive film on the 316 SS surface probably undergoes breakdown rather than re-passivation, leading to

[a]*Future Materials & Devices Lab., Institute of Fundamental and Applied Sciences, Duy Tan University, Ho Chi Minh City 70000, Vietnam. E-mail: nguyenngocnhi8@duytan.edu.vn*

[b]*The Faculty of Environmental and Chemical Engineering, Duy Tan University, Danang 55000, Vietnam*

[c]*Ho Chi Minh City University of Technology and Education, Ho Chi Minh City 70000, Vietnam*

[d]*Southern Branch of Joint Vietnam-Russia Tropical Science and Technology Research Center, 3, 3/2 Street, Vuon Lai Ward, Ho Chi Minh City, Vietnam*

[e]*Department Petroleum Geology and Reservoir Engineering, Petroleum-Gas University of Ploiesti, Ploiesti, Romania*

a significant loss in corrosion resistance.[7] To deal with those negative effects, some methods are employed to reinforce this SS passive layer, such as thermochemical diffusion,[16,17] anodization[18] or acid-based passivation.[19] In which, thermochemical diffusion treatments and anodization do have some advantages to be utilized in metallurgy field, but they still have shortcomings associated with the saturation process of N on the steel surface and controlling morphology. These methods frequently require a long-time treatment of up to 10 hours and cause variations in pore size and shape of surface structure due to the use of the high voltage. Among them, the easiest and the most effective way is the use of acid-based passivation technique that involves using a mild oxidant to remove heterogeneous passive layers on the metal surface for the formation of a new more compact passive film.[19,20] In this approach, the commonly used acidic solution is nitric acid (HNO_3) for its passivating effect,[21,22] but it raises environmental concerns due to the generation of NO_x gases and nitrite byproducts during process. Sulfuric acid (H_2SO_4) is another acid commonly employed in acid-based passivation of SS, where it not only removes surface contaminants and dissolves free iron/iron oxides but also facilitates the regeneration of a cleaner, chromium-enriched surface that can repassivate more effectively, resulting in enhancing the overall corrosion resistance of 316 SS.[19,23] Unfortunately, despite the improvements achieved through passivation, the passive film remains vulnerable under prolonged exposure to aggressive environments. This deterioration arises from its inherently limited structural integrity, the presence of inclusions or localized defects that compromise its long-term stability. In this study, inspired by ability of acidic treatment to reconstruct and rejuvenate the surficial passive film, and recognizing the inherent microstructural limitations that make this film vulnerable to degradation under harsh environments, we combine sulfuric acid (H_2SO_4) treatment with deposition of a polymer coating on the SS surface. This integrated approach aims to mitigate passive-film breakdown and enhance the long-term corrosion resistance of 316 SS in seawater.

Recently, conducting polymers (CPs) have been widely investigated due to their extraordinary advantages over traditional types, including high mechanical stability, ease in material processing, and especially tunable electrical conductivity.[24] Based on those advantages above, CPs have emerged as preferred material class for a wide range of applications. Among them, corrosion-resistant coatings are particularly prominent, as CPs uniquely combine electrochemical activity with effective barrier protection.[25,26] More specifically, polyaniline (PANi) is selected because its π-conjugated backbone supports the delocalization of charge carriers, and upon protonic doping, this structure enables efficient electron transport, resulting its well-known intrinsic conductivity.[27–30] This redox-active nature allows PANi to participate directly in passivation process, where its reversible oxidation states can promote the regeneration and stabilization of the passive film on SS, so enhancing corrosion protection through a redox-mediated mechanism. Therefore, PANi is considered a fundamental polymer due to its responsive redox behavior, high environmental stability, proven effectiveness in corrosion protection for various metals, including copper,[31] aluminum,[32] carbon steel, iron,[33] and stainless steel.[30,34] Chemically, PANi can exist in three main oxidation states including: leuco-emeraldine base (LEB), emeraldine base (EB), and pernigraniline base (PAB), each corresponds to a different oxidation level of the amine functionalities within the polymer back bone. Transitions among these states are pH-dependent and underpin the reversible redox behavior that enables PANi to participate in passivation and interfacial electrochemical processes.[35] However, its protective capability decreases over prolonged immersion in aqueous environments since the intrinsic porosity of PANi allows aggressive species, particularly chloride ions, to diffuse through the coating and reach the underlying metal surface. This limitation highlights the need for a complementary strategy, in which surface treatment in a 1 M H_2SO_4 solution first reconstructs a cleaner and more stable passive film, while the subsequent PANi coating provides redox-mediated reinforcement and additional barrier protection. Furthermore, acidic solution helps increases surface energy, aiming to not only increase corrosion resistance of 316 SS but also enhance the bonding of PANi coating with the SS surface for an enhanced film structure.

2. Experiment section

In this study, dark polyaniline (PANi) powder (the mean $M_w \sim 50\,000 \div 60\,000$) and dimethyl sulfoxide 99.9% (DMSO) as a diluting solvent is provided by Fisher America (Cas 67-68-5). Two of which can be used directly without further purification. The PANi-based solution as a coating material for spin coating process was prepared according to the following procedure: (1) 0.1 g PANi powder was dissolved in 9.9 g DMSO solution, then continuously stirred within 1 h using an ultrasonic technique to minimize polymer agglomerates. After that, the mixture solution was stirred continuously for next 24 h at the room temperature before filtration using a 0.3 μm filter paper. This process was applied to make sure that insoluble solid impurities were removed from the solution. After that, the solution was aged for few hours to stabilize before coating. Additionally, a 54.39 mL of 98% H_2SO_4 solution provided by Sigma-Aldrich was diluted with a 1 L of dilute water to obtain 1 M solution, used as a treatment solution. Additionally, 316 SS specimens were machined into a fixed dimension ($1.5 \times 1.5 \times 0.3$ cm) were grinded by SiC abrasive papers with grit sizes (100, 600, 1000, and 2000) to remove surface irregularities and obtain a smooth, uniform surface for subsequent treatment. The ground samples were then cleaned with diluted water and rinsed with ethanol to remove residuals, finally dried by a hairdryer.

In the next step, the prepared SS sample was treated in the 1 M H_2SO_4 solution within 1 h to facilitate the formation of a new oxide layer as a physical barrier and a buffer layer for enhancing the adhesion of PANi coating on the SS surface. To evaluate these effects of surface treatment, both the untreated and treated samples covered with PANi using a spin coating technique were assessed to have a comprehensive figure. In this study, the spin-coating process was conducted through a CY-SPC8-H spin coater, established with four main stages.[36,37] At stage I, 0.1 mL of the prepared PANi solution was dropped on

the substrate at the static state. At the stage II, the sample was spin-coated at 500 rpm for 5 s, followed by acceleration to 1000 rpm, which was maintained for 15 s to ensure uniform spreading of the coating solution across the SS surface. This stage is known as spin-up. In the next stage, the spinning speed was increased to 2000 rpm and maintained for 30 s to control the film thickness, followed by a further acceleration to 3000 rpm for 15 s to complete the thinning and uniformization of the coating layer. In the final stage, the rotation speed was increased to 4000 rpm and maintained for 5 s to achieve a uniform, smooth, and well-adhered coating on the 316 SS surface, corresponding to the spin-off. After spinning, the PANi-coated samples were placed in a chamber with silica gel to prevent moisture absorption. This is because PANi is relatively sensitive to moisture, which can significantly affect its conductivity and morphology, since moisture leads to unwanted chemical changes in PANi. So, this step helps stabilize the coated samples before further characterization.

The samples in four treatment conditions, including (#1) reference specimen (solely ground 316 SS surface), (#2) ground and treated 316 SS surface in the 1 M H_2SO_4 solution, (#3) PANi-coated and untreated 316 SS surface, and (#4) PANi-coated and treated 316 SS surface, were characterized by both electrochemical measurements and surface characterizations. For electrochemical measurements, all of which were undertaken using a three-electrode system, including a working electrode (a target metal candidate, WE), a Ag/AgCl reference electrode (RE) filled with a saturated KCl solution used to monitor the potential of the WE, a counter electrode (CE) for balancing the electrochemical system. Three electrodes were completely immersed in a 3.5 wt% NaCl solution and connected with a Parstat and VSP system to control external load and record electric responses. First of all, open circuit potential (OCP) were conducted for 1 h before each electrochemical measurement to stabilize the electrochemical system and record the time-variant potential. Second, potentiodynamic polarization (PD) test was set up with the starting potential from −250 mV *vs.* OCP to the final potential where the current density reaches 10^{-3} A cm^{-2} at a consistent scan rate of 0.166 mV s^{-1}. Third, electrochemical impedance spectroscopy (EIS) were established at the sinusoidal perturbation being of ±10 mV and the frequency window ranging from 100 kHz to 10 mHz. During EIS, OCP re-scan every 2 h during 168 h of immersion in the testing solution.

For surface characterizations, specimens in four conditions were immersed in the 3.5 wt% NaCl solution for 168 h at OCP. After that, field emission scanning electron microscopy (FE-SEM, Hitachi TM3030Plus) were employed to observe surficial morphologies and measure coating thicknesses. Additionally, topological features of the untreated and treated 316 SS surfaces were analyzed by atomic force microscopy (AFM, Agilent 5500 AFM) to clarify the function of acidic treatment in improving surficial features of 316 SS. After that, the results obtained from AFM were processed using statistical quantity software to extract quantitative surface parameters. In particular, some parameters including average roughness, root mean square roughness (rms), and peak-to-valley height, as well as average surface roughness of the samples were calculated from 2D and 3D mappings. Additionally, the contact angle (CA) method was applied to predict the wettability and surface energy of SS surfaces using OCA-20 ES (Data Physic, Germany). During analysis, each sample was measured at least at 3 points, and the electrolyte (3.5 wt% solution) droplet is 7 μl. It is noticed that if the difference of CA measurements on the same sample surface are within 5°, the average value is calculated. Chemical coating compositions before and after 168 h of immersion in the testing solution were also analyzed using attenuated total reflectance Fourier-transform infrared spectroscopy (ATR-FTIR, Alpha II – platinum FTIR spectrometer). ATR-FTIR analysis involved the direct contact between the sample surface and the ATR crystal, where an infrared light is directed onto the sample and the spectra are collected in the wavenumber range of 4000 ÷ 600 cm^{-1} at room temperature.

3. Results and discussion

3.1. Surface analysis

Fig. 1 shows SEM and cross-section images of specimens in four conditions (#1 ÷ #4) before immersion in a 3.5 wt% NaCl solution, showing changes in morphological features and thickness of coating before and after acidic treatment and coating. In general, SS surfaces in all conditions remains flat and uniform, with no evident defect sites observed, expect for the presence of remaining grinding marks. More specifically, the sample #1 (Fig. 1(a)) exhibits grinding marks. Meanwhile, the sample #2 (Fig. 1(b)) still has grinding marks but the overall morphology is smoother and more homogenous, suggesting that the formation of a passive layer contributes to surface uniformity. For the sample #3 (Fig. 1(c)), the remaining grinding marks are obvious, although the substrate surface was coated with PANi. This indicates that the polymer layer conforms to the surface morphology of the SS rather than masking its mechanical features, with no evidence of mark filling. Therefore, the PANi coating exhibits a highly rough and porous structure, with localized contrast observed in the SEM images. These variations are likely associated with nodular growth, polymer aggregation, or surface charging effects during SEM imaging. For the sample #4 (Fig. 1(d)), the presence of white spots on the surface reduces significantly, indicating the combined surface treatment and polymer coating result in a more uniform coating morphology. This observation underscores the critical role of surface finish in enhancing the surface quality of SS prior to PANi coating. Unlikes the surface #1, which retains visible scratches and slight surface irregularities, the acid-treated samples exhibit a smoother morphology. Fig. 1(e and f) represents the cross-sectional image of the PANi coating on the untreated and treated 316 SS surfaces. The coating thicknesses were estimated to be approximately 417.11 ± 9.78 nm for the untreated surface and 523.28 ± 30.06 nm for the treated surface.

Additionally, topological features of the untreated and acid-treated SS specimens were analyzed by AFM, displayed by both 2D and 3D mappings, as shown in Fig. 2(a and b). Correlating with the results from the SEM images, the 2D and 3D topographical mappings show that the sample #2 exhibits a more

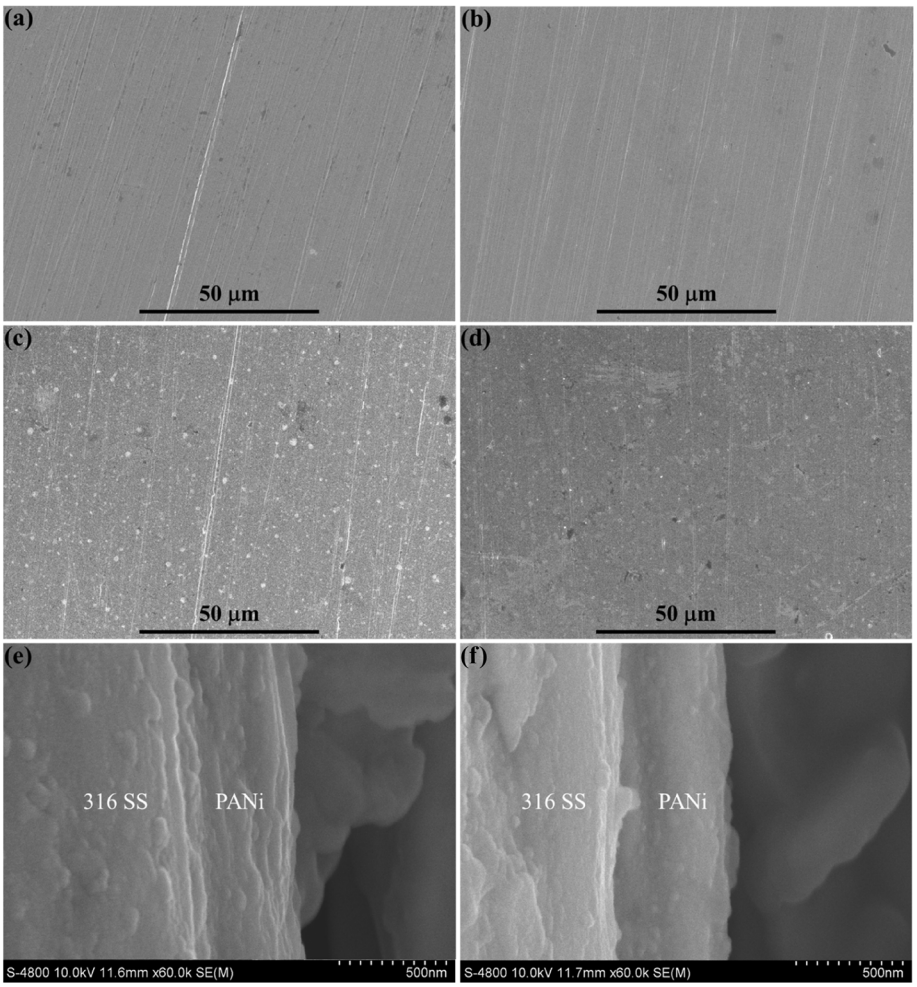

Fig. 1 Surface morphology of (a) ground 316 SS surface and (b) ground and treated 316 SS surface, and PANi-coated on (c) ground 316 SS and (d) ground and treated 316 SS. The coating thickness of PANi coatings (e) ground 316 SS and (f) ground and treated 316 SS.

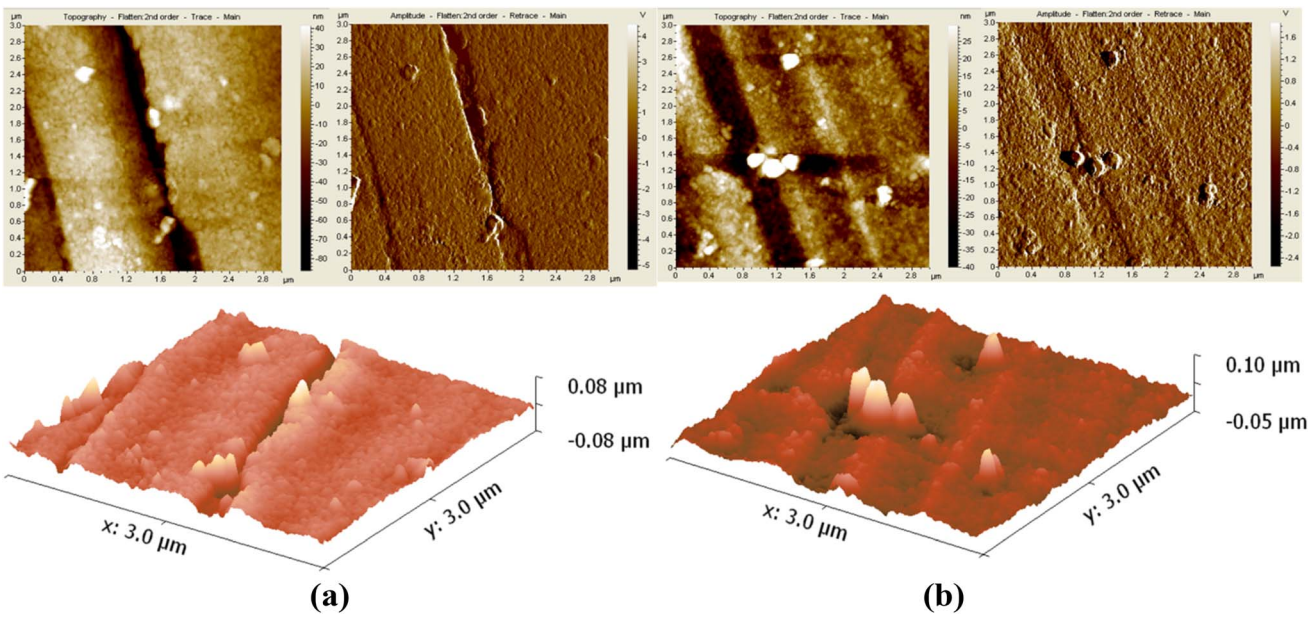

Fig. 2 AFM results of 316 SS after (a) ground surface and (b) ground surface treated in 1 M H_2SO_4 solution for 1 h.

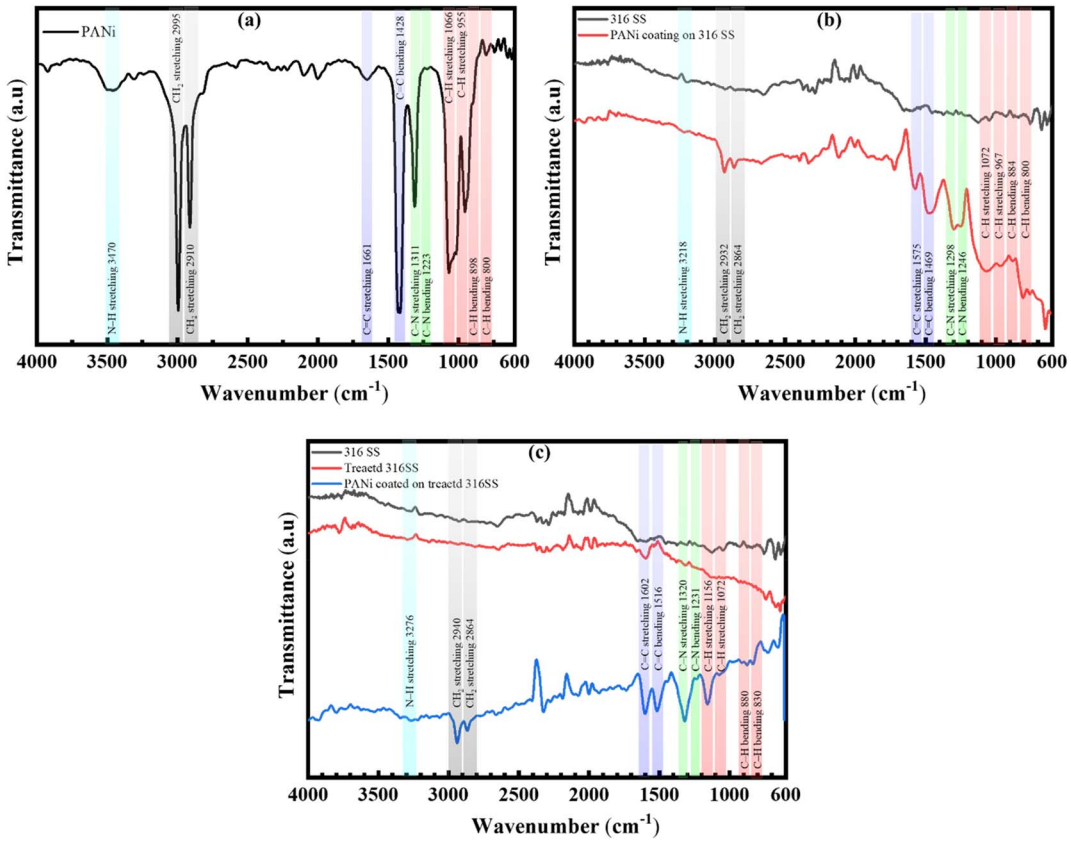

Fig. 3 Attenuated total reflectance-Fourier transform infrared (ATR-FTIR) spectroscopy of (a) PANi as raw material, (b) PANi coating on the ground 316 SS surface, and (c) PANi coating on the ground, treated 316 SS surface.

homogeneous morphology compared to the sample #1. In this regard, the grinding marks are clearly visible on the untreated surface, with the deepest groove reaching 0.08 μm, whereas on the treated surface the maximum groove depth decreases to 0.05 μm. This reduction in groove depth is attributed to the formation of a thin passive layer that initially fills surface defects and modifies the near-surface microstructure during immersion in the 1 M H_2SO_4 solution within 1 h. This phenomenon can be explained by the dual-layer passive film model commonly proposed for passivating metals,[38] in which the passive film consists of a dense inner oxide layer and an outer porous oxo-hydroxide layer, each performing a distinct function in filling surface defects and smoothing the microstructure. In essence, chromium readily forms a dense and adherent chromium oxide layer on the SS surface. During passivation, chromium atoms diffuse toward the surface and undergo selective oxidation, facilitating the development of a compact inner barrier layer that governs the alloy's corrosion resistance. Meanwhile, iron-related species tend to occupy defect sites or migrate toward through vacancy pathways within the passive film. As a result, Fe-oxides and hydroxides preferentially accumulate in the outer region of the passive film, where defect density and ion transport are higher. This defect-mediate redistribution contributes to the smoother surface observed after acidic treatment, as the passive film partially fills the grinding marks, leading to a measurable reduction in groove depth.

ATR-FTIR spectroscopy was recorded in the wavenumber range from 600 to 4000 cm^{-1} to analyze the functional groups in PANi powder and on the 316 SS surfaces in four conditions, with particular focus on identifying PANi through its characteristic vibrational modes. Firstly, Fig. 3(a) represents the spectrum of PANi powder, which is used as the reference spectrum. In particular, a characteristic adsorption peak appears at 3470 cm^{-1}, corresponding to the N–H stretching vibration of secondary amine groups in the PANi backbone. This peak serves as a key spectral signature confirming the presence of PANi. Additionally, the adsorption peaks at 2995 and 2910 cm^{-1} correspond to the asymmetric and symmetric C–H stretching modes of CH_2 groups, respectively. These features are typical of aliphatic hydrocarbon vibrations and further support the identification of aliphatic components within the sample.[39] These vibrational modes commonly appear in PANi due to its side-chain environment and structural units, supporting the identification of the polymer. They are characteristic of the benzenoid (–NH–C_6H_4–NH–) and quinoid (=N–C_6H_4–N=) segments, which correspond to the reduced and oxidized forms of PANi, respectively. Typically, the characteristic peaks at 1428 and 1661 cm^{-1} arise from the C=C stretching modes of the benzenoid and quinoid rings, respectively. Their alternating arrangement along the PANi chain facilitates π-electron

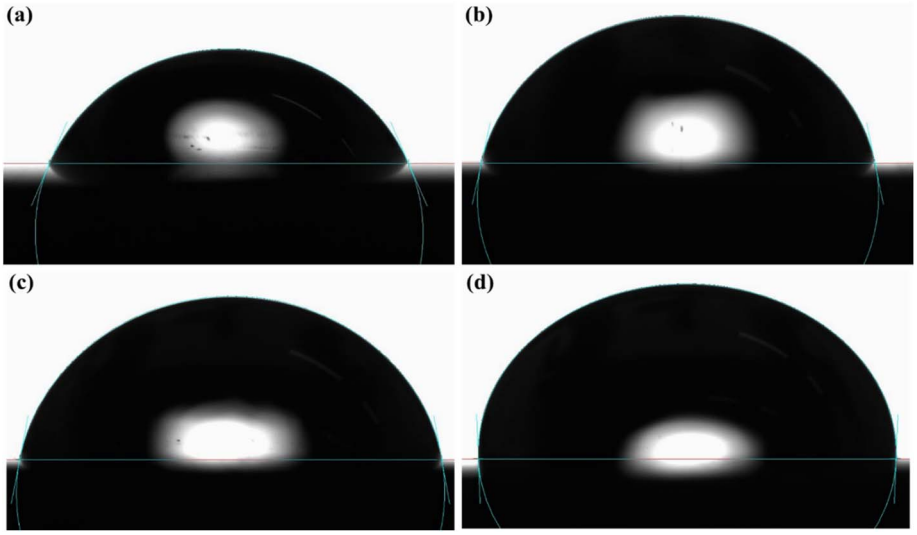

Fig. 4 Contact angle results of (a) ground 316 SS surface and (b) ground and treated 316 SS surface, and PANi coating on (c) the ground 316 SS and (d) the ground and treated 316 SS.

delocalization, forming the conjugated pathway responsible for the polymer's electrical conductivity. These bands are characteristic of the emeraldine base, the partially oxidized form of PANi in which benzenoid and quinoid units coexist in a balanced ratio.[40] Furthermore, peaks located at 1311, 1223, 1066, 955, 898, and 800 cm^{-1} represent characteristic C–N stretching and C–H bending vibrations within the PANi backbone, reflecting the presence of benzenoid and quinoid as well as ring deformation modes. All the observed peaks in the FTIR spectrum of PANi powder show the agreement with the spectral features of PANi reported by other researchers in the previous literature.[41,42] In Fig. 3(b), the FTIR spectrum reveals distinct differences between the samples #1 and #3. It is obvious that the sample #1 exhibits a broad, low-intensity spectrum with no detectable signals associated with organic compounds. In contrast, the sample #3 displays well-defined peaks that closely resemble the molecular fingerprint of PANi powder, although slight shifts toward lower wavenumbers are observed. This minor wavenumber shift may arise from the interfacial bonding or electronic interactions between the PANi chains and the thin passive oxide layer on the SS surface.[43] These interactions can slightly weaken specific bonds (C–N, N–H, C=C), thereby lowering their vibrational frequencies and producing the observed shift toward lower wavenumbers. Additionally, the amine and imine groups in PANi are capable of forming hydrogen bonds with hydroxyl groups on the SS surface, which further reduces bond strength and consequently decreases vibrational energy. Beyond these effects, conformational adjustments of the PANi backbone upon adsorption also include subtle distortion in bond angles and lengths, contributing to the downward shift in peak positions. Such shifts are indirect evidence of chemical and physical bonding between the polymer and the substrate, which significantly affect the interfacial properties and the electrochemical response of the coated system. Fig. 3(c) provides the FTIR spectra of three samples #1, #2, and #4. In the spectrum of the sample #2, no new peak is clearly observed as compared to that of the specimen #1. On the sample #4, the observed peaks are similar to those of the sample #3, indicating that PANi deposits effectively on the SS surface regardless of whether the substrate is untreated or acid-treated.

In the context of CA measurement, it was applied to examine the wettability of four samples in a 3.5 wt% NaCl solution and to point out the role of surface finish on the improvement of surface characteristics. Fig. 4 and Table 1 summarize the results obtained from the CA measurement, where the CA of the sample #4 exhibits the highest value of around 90°. According to Young's model of wettability,[43,44] the CA is less than 90°, meaning that the liquid tends to spread over the surface, indicating that the surface is hydrophilic. This occurs when the solid–liquid interfacial energy is lower than the solid–gas interfacial energy, promoting wetting. It clearly show that the sample #1 exhibits the average CA of about 66°, indicating that the surface interacts more readily with the liquid compared with surfaces exhibiting higher CAs. This behavior may be attributed to the effect of grinding process, which reduces surface roughness and eliminates micro-crevices that would otherwise contribute to higher apparent hydrophobicity. For the sample #2 (Fig. 4(b)), the CA increases to 82°, demonstrating enhanced hydrophobicity relative to the sample #1. This

Table 1 Contact angle results extracted form the angle of droplet of the 3.5 wt% NaCl solution

Sample	316 SS	Treated 316 SS	PANi coating on 316 SS	PANi coating on treared 316 SS
#1	66°	82°	76°	88°
#2	68°	81°	80°	91°
#3	65°	84°	79°	92°
Contact angle	66°	82°	78°	90°

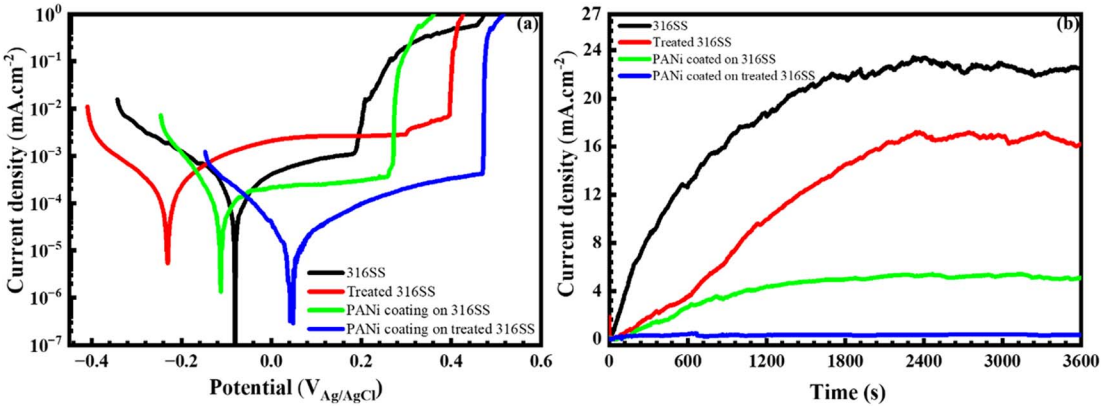

Fig. 5 (a) Representation of potentiodynamic polarization and (b) potentiostatic polarization tests of the samples at anodic applied potential of +400 $mV_{Ag/AgCl}$ in the 3.5 wt% NaCl solution.

behavior arises from the acidic treatment, which can subtly reorganize the passive film or modify the micro-/nano-scale roughness. In particular, the treatment process creates a passive layer on the 316 SS surface (Cr_2O_3, Fe_2O_3 or Fe_3O_4) that reduce the number or hydrophilic surface sites and thus lower the surface's affinity for water.[45–47] In Fig. 4(c and d) of the CA of the coated systems, the sample #4 exhibits the highest average CA of approximately 90°, suggesting a transition toward a more hydrophobic surface. This enhancement in hydrophobicity can be attributed to the combined effects of acidic treatment and the presence of the PANi coating. In which, the porous PANi coating introduces hierarchical surface features capable of retaining air within the pores that promotes a Cassie–Baxter wetting regime, effectively lowering the liquid–solid contact fraction and increasing the apparent contact angle.

3.2. Electrochemical characterizations

To evaluate the effect of acidic treatment and PANi coating on the electrochemical activity of 316 SS as immersed in the 3.5 wt% NaCl solution, electrochemical measurements were conducted. For stabilizing the electrochemcial system, OCP was conducted before 1 h. After that, PD test was undertaken and the results obtained were given in Fig. 5(a) and Table 2. The PD results were presented in the form of Tafel plot, in which anodic branches represent for metal dissolution, passivation, and breakdown, while cathodic branches are controlled by reduction reactions. In general, PD results reveal a clear difference among the four samples, including variations in current density, corrosion potential, and especially pitting/breakdown corrosion. More specifically, at anodic branches just above OCP, the current density increases significantly, reflecting the onset of initial metal dissolution from the SS surface. In the case of the system #1, a rise in current density indicates that the protective film is barely developed, allowing metal dissolution (Fe, Cr, Ni, *etc.* ions) into the electrolyte. After the initial dissolution, the current density decreases over the applied potential and stabilizes as the passive film thickens, marking the transition from active dissolution to passivation. This phenomenon is observed at all four cases, indicating that it is a general behavior of 316 SS in the seawater. Although the treatment significantly influences the magnitude and kinetics of dissolution, the fundamental process of transient metal ion release prior to passive film stabilization remains unavoidable. Furthermore, the pitting potential (E_{pit}) shows a pronounced shift among different conditions, with the PANi-coated/treated specimen (sample #4) achieving the highest E_{pit}. This improvement reflects the synergistic effect of acidic treatment and the protective PANi coating, which together delay passive-film breakdown more effectively than the sample #1. In which, acidic treatment is responsible for enriching passive layers, while PANi coating provides an additional barrier and electroactive protection, thus contributing the strongest resistance to pit initiation. In the context of cathodic branches, acidic treatment and PANi coating significantly influences reduction reactions (oxygen reduction or hydrogen evolution) at the surface, when the cathodic current density varies significantly across conditions. A clear shift of the cathodic region is

Table 2 Corrosion parameters extracted from potentiodynamic polarization in 3.5 wt% NaCl solution

Sample	E_{corr} ($mV_{Ag/AgCl}$)	i_{corr} ($\mu A\ cm^{-2}$)	β_a ($mV\ decade^{-1}$)	$-\beta_c$ ($mV\ decade^{-1}$)	i_{pass} ($\mu A\ cm^{-2}$)	E_{pit} ($mV_{Ag/AgCl}$)	ΔE ($mV_{Ag/AgCl}$)	Protective efficiency (%)
316 SS	−80.9 ± 2.87	0.131 ± 0.070	163	89	1.126 ± 0.104	187 ± 15.5	267.9	—
Treated 316 SS	−236.3 ± 13.1	0.060 ± 0.003	61	44	2.627 ± 0.352	396 ± 25.5	632.3	—
PANi coating on 316 SS	−112.9 ± 2.35	0.032 ± 0.003	58	35	0.384 ± 0.020	259 ± 22.0	371.9	75.6 ± 2.0
PANi coating on treated 316 SS	44.90 ± 2.70	0.007 ± 0.001	85	64	0.293 ± 0.049	469 ± 20.2	424.1	94.7 ± 0.9

observed, with the sample #4 exhibiting the most pronounced positive displacement together with the lowest current density. Such a positive displacement means that a less negative potential is required to drive the same level of cathodic current, reflecting the growing difficulty of initiating oxygen reduction or hydrogen evolution at the surface. This behavior demonstrates that the acidic treatment, and more prominently, the PANi coating effectively hinders electron transfer and reduces the availability of electroactive sites for cathodic reactions. To have a comprehensive and objective assessment, electrochemical parameters, including corrosion current density (i_{corr}), corrosion potential (E_{corr}), anodic/cathodic Tafel slopes (β_a, $-\beta_c$), pitting potential (E_{pit}) are extracted by Tafel extrapolating, as summarized in Table 2. Based on the current density obtained at each condition, the protective efficiency (P_i) of the coatings is determined using the following equation:[48]

$$P_i(\%) = 100 \times \left(1 - \frac{i_{corr}}{i^o_{corr}}\right) \quad (1)$$

where i_{corr} and i^o_{corr} are the corrosion current densities of the samples with and without pretreatment and coating, respectively.

The results obtained from linear extrapolation show that the corrosion current density of the pretreated and coated samples is significantly reduced compared to the sample #1. In particular, the sample #4 shows an i_{corr} value of only 0.007 ± 0.001 (μA cm^{-2}), which is indicative of a highly inhibited corrosion process. Such a low current density suggests that the PANi layer provides dual protection: (i) a physical barrier effect that restrict electrolyte penetration and reduces the number of exposed active sites, and (ii) a redox-mediated stabilization of the passive film, which suppressed metal dissolution and maintains a low passive current density during polarization. Table 2 shows the protective efficiency of the electrochemical system is high up to $94.7 \pm 0.9\%$ for the PANi-coated/treated 316 SS. Moreover, the E_{pit} value of this sample reaches the highest among all the conditions, indicating that the PANi coating on the treated 316 SS surface provides the most effective resistance against pitting corrosion.

Based on PD results obtained, an anodic potential of +400 $mV_{Ag/AgCl}$ was selected within the passive potential regime of the specimen #4 to evaluate the stabilization of the surface covered by the passive layer and the PANi coating. This potential lies well above the corrosion potential yet remains below the pitting initiation threshold, allowing the assessment of how effectively the combined passive layer and PANi coating withstand sustained anodic polarization without undergoing localized breakdown. As shown in Fig. 5(b), the anodic current densities of the samples #1 ÷ 3 exhibit an initial rise within the first few seconds and then remain at relatively high and unstable levels throughout the testing time. This behavior indicates that the SS surfaces are unable to maintain a stable passive state under the applied potential, leading to the progressive passive film degradation and ultimately to localized breakdown, as reflected by the sudden sharp increase in current density. In contrast, the sample #4 maintains a small and highly stable anodic current

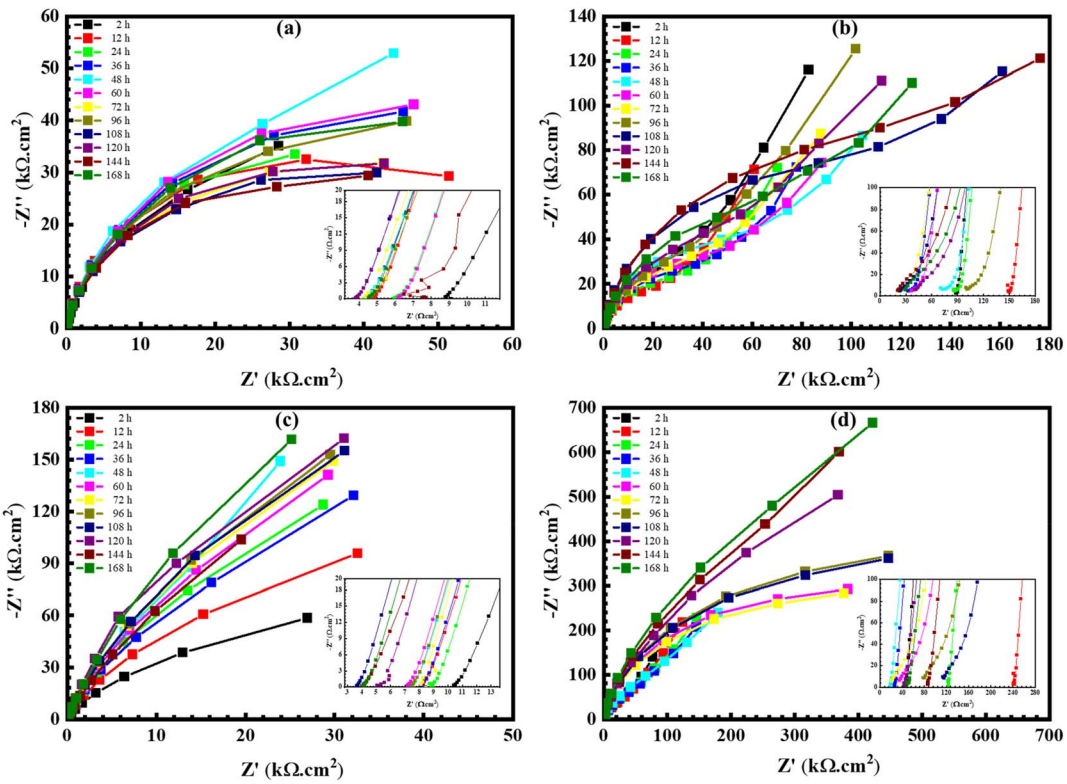

Fig. 6 Nyquist plots for EIS data during 168 h immersion in 3.5 wt% NaCl solution of (a) ground 316 SS surface and (c) ground and treated 316 SS surface, and PANi coating on (b) the ground 316 SS and (d) ground and treated 316 SS.

density during the testing period. It is consistent with the PD results, and together they indicate that the passive film and PANi coating on this sample remains intact under the applied anodic stress. The PANi coating effectively reinforces the passive layer, preventing its degradation and thereby sustaining a low passive current density during polarization.

To analyze the electrochemical processes at the electrode/electrolyte, EIS was carried out during 168 h immersion in a 3.5 wt% NaCl solution and the results were displayed by Nyquist plots in Fig. 6. The diameter of the semicircle corresponds to the charge transfer resistance (R_{ct}), which is directly related to corrosion resistance. A larger semicircle indicates higher R_{ct}, reflecting slower electron transfer kinetics and enhanced stability of the passive film, thereby improving the alloy's resistance to localized corrosion. To better understand the meaning of the Nyquist diagram, the frequency regions corresponding to each process on the sample surface are divided into three regions: (1) the high-frequency region representing the solution resistance and the interface of electrolyte/electrode, (2) the medium-frequency region related to the process within passive and coating layers, and (3) the low-frequency region indicating processes at the metal/coating interface. In general, although $-Z''$ has changed, both Z' and $-Z''$ still remains at a high level at the medium and low frequency regions, indicating that the system still maintains a passive state and effective protection against the seawater environment, despite degradation from chloride ion attack over the extended exposure period. In the case of the system #1 (Fig. 6(a)), it exhibits a large semicircle in the first immersion hours and tends to expand over 48 h immersion, meaning that the polarization resistance increases due to the formation of a stable, natural passive film. After 48 h immersion, semicircular loops become slightly depressed, but the charge-transfer resistance remains at a high value. It indicates that although surface heterogeneity increases, likely due to localized dissolution and passive-film roughening, the passive layer is still largely preserved and continues to provide significant resistance to charge transfer. In the case of the specimen #2 (Fig. 6(b)), arc diameters in Nyquist plot increases significantly, nearly 2 ÷ 3 times compared to the untreated case #1, indicating a major improvement in corrosion resistance. This suggests that the surface treatment promoted the formation of a denser, more protective passive film that reduces charge transfer across the interface. Besides, the $-Z''$ value becomes more negative in the low-frequencies region, indicating the dominance of capacitive behavior and diffusion-controlled processes at the electrode/electrolyte interface. This is often associated with the growth or stabilization of the passive film, which behaves like a dielectric barrier that resists rapid electron exchange. For the system #3 (Fig. 6(c)), a large difference is observed compared with the system #1. The $-Z''$ values become significantly more negative, reaching nearly -170 k$\Omega.cm^2$, while the Z' values decreases. This behavior reflects the stronger capacitive response induced by the PANi layer and the suppression of resistive pathways at the interface. These features indicate that the polymer coating alters the interfacial

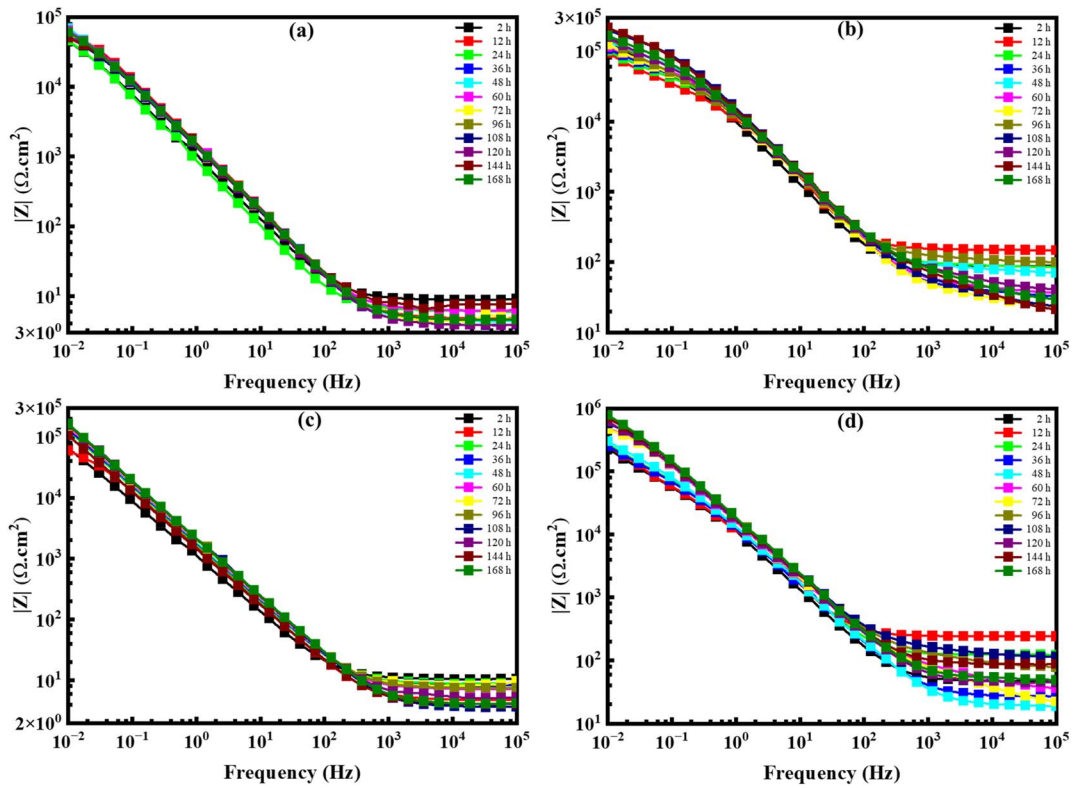

Fig. 7 Bode plots for EIS data during 168 h immersion in 3.5 wt% NaCl solution of (a) ground 316 SS surface and (c) ground and treated 316 SS surface, and PANi coating on (b) the ground 316 SS and (d) ground and treated 316 SS.

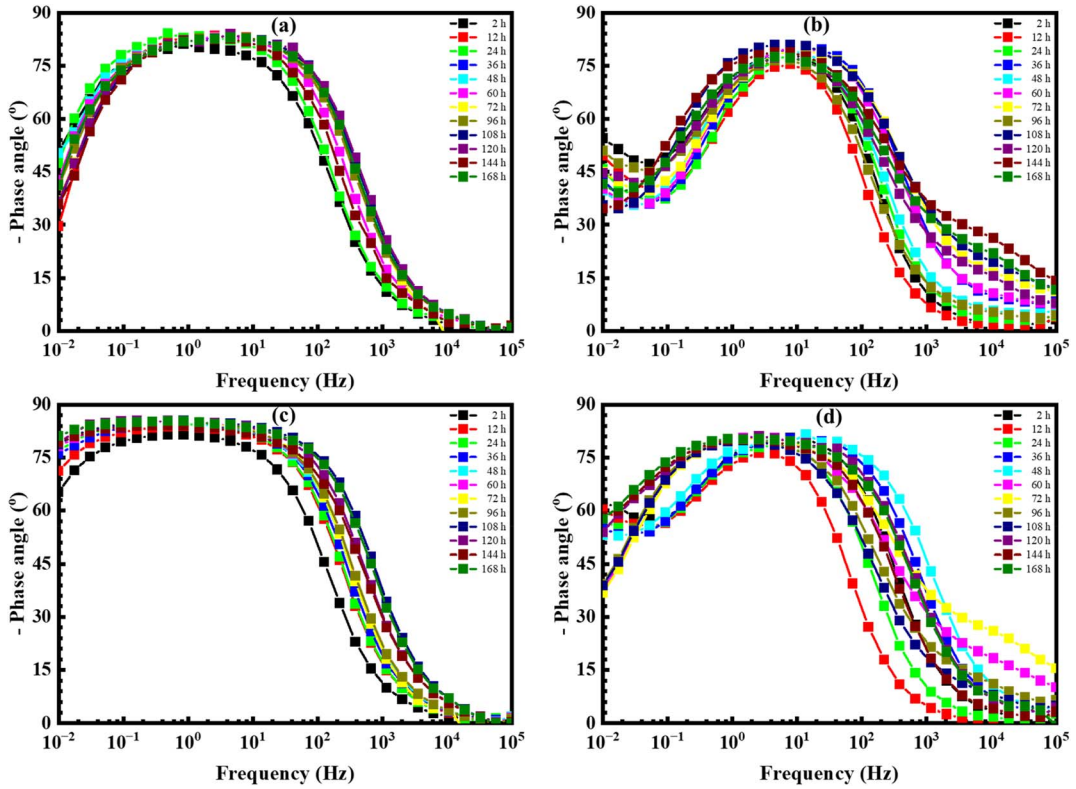

Fig. 8 Bode phase plots for EIS data during 168 h immersion in 3.5 wt% NaCl solution of (a) ground 316 SS surface and (c) ground and treated 316 SS surface, and PANi coating on (b) the ground 316 SS and (d) ground and treated 316 SS.

electrochemical processes, even in the presence of prior surface pretreatment. More specifically, a more negative Z'' shows a greated capacitive contribution where the system is storing charge more efficiently. It reflects the ability of the PANi coating to impede ion migration and slow down interfacial corrosion reactions. In parallel, Z' component represents the resistive element of the system, including solution resistance, film resistance, and charge transfer resistance, providing insight into how the coating modifies the overall electrochemical response.

Different from the behavior of the system #3, the specimen #4 experiences a pronounced increase in both Z' and negative Z'', much higher than those of the other cases. This demonstrates that both acid treatment and PANi coating enhances both resistive and capacitive effects, reflecting superior interfacial stability and corrosion resistance. It could be suggested that acidic treatment enriches the passive film and introduces active surface groups, which may enhance interfacial interactions with PANi and contribute to improved barrier properties. More interestingly, Z' and negative Z'' values tend to increase over immersion time, reflecting the coating becomes increasingly effective at storing charge and the growing impedance to ionic and electronic transport. As a result, these features confirm that the PANi-reinforced passive film continues to stabilize and strengthen during prolonged immersion.

In addition, Bode plots in impedance magnitude form ($|Z|$) and phase angle (°) are represented to provide a comprehensive view of the frequency-dependent electrochemical behavior of the system that is not fully represented on Nyquist plots (Fig. 7 and 8, respectively). It can be seen in Fig. 7(a), the impedance value of the system of the sample #1 at a low frequency of 10^{-2} Hz remains at a high value of 10^5 (Ω cm^2) for 168 h, yet this is the lowest among all tested cases, obviously demonstrating a weaker barrier compared to the acid-treated and PANi-coated specimens (3×10^5 Ω cm^2 for the specimens #2 and #3 and 10^6 Ω cm^2 for the specimen #4). This high impedance magnitude at low frequencies reflects the ability of the surface to resist long-term charge transfer and ion diffusion, confirming their superior protective performance. At a medium-frequency region (10^0 to 10^2 Hz) of all four conditions, $|Z|$ reduces linearly, indicating that the response is dominated by interfacial polarization governed by charge transfer resistance and double-layer (or coating) capacitance. The linear trend in $\log|Z|$ *vs.* frequency reflects a non-ideal capacitive behavior often modeled as a constant phase element (CPE). A clear and consistent linearity suggests a uniform, stable passive film/coating, particularly evident in the two coated systems, where the impedance response reflects enhanced interfacial homogeneity and superior barrier properties. Finally, in a high-frequency region, the impedance is primarily controlled by the ohmic elements of the system, namely the solution resistance and the intrinsic resistance of the coating. Under these conditions, the capacitive behavior of the interface is minimal because of the rapid AC perturbation does not allow sufficient time for charge accumulation at the coating/electrolyte interface. At this region, the alternating current passes through the electrolyte with minimal

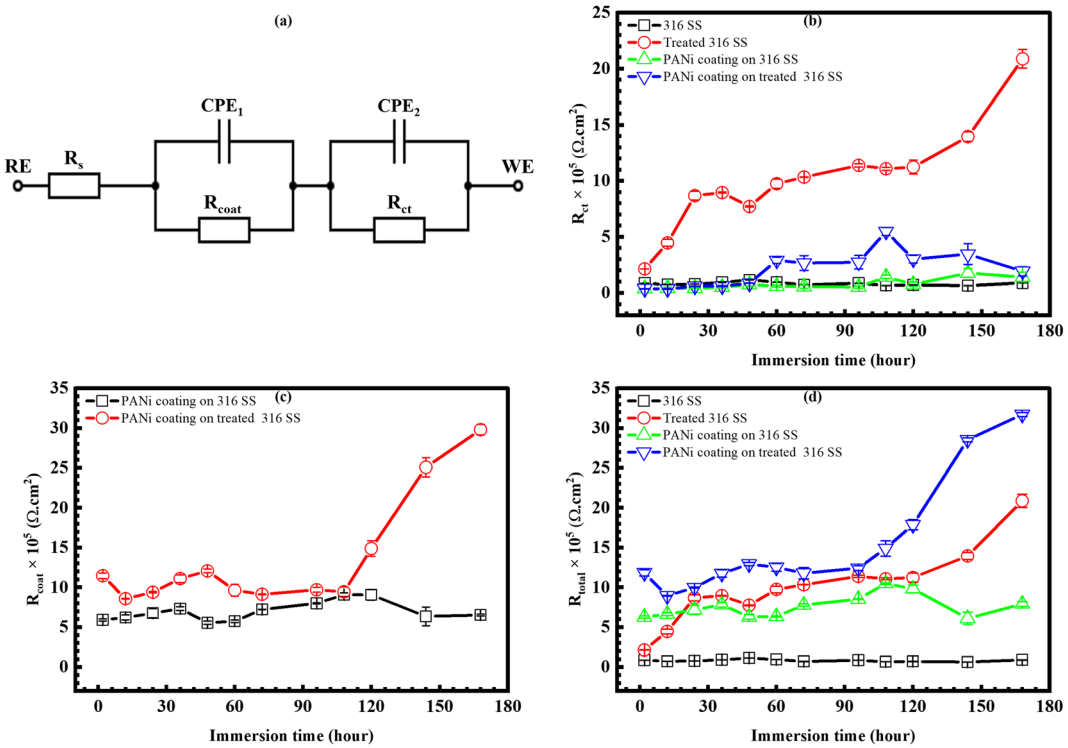

Fig. 9 (a) Equivalent circuit used to fit the EIS data and time-variant resistance for 7 day immersion including: (b) charge transfer resistance, (c) the surface film/coating resistance and (d) total resistance.

polarization and it is determined by the conductivity of the NaCl solution. The $|Z|$ values at the high-frequency region vary within $10 \div 100\ \Omega\ cm^2$ over immersion time, reflecting the dominance of solution resistance and minor coating resistance. This narrow variation confirms that capacitive contributions are negligible at high frequency, and the impedance response is largely controlled by the electrolyte conductivity rather than interfacial polarization. This variation within the range from 10 to 100 $\Omega\ cm^2$ is observed clearly in the two cases of treated and coated/treated specimens. This is probably because the acidic treatment produces a compact oxide-rich passive film, while the PANi coating adds an additional resistive barrier, thus elevating and stabilizing the high-frequency impedance response beyond the solution resistance. Additionally, the slope at peak, correlating phase angle (Fig. 8), marks the frequency at which the system transitions between resistive and capacitive behaviors. Based on the shape of phase angle plots, it suggests multiple overlapping time constants, particularly in the systems #1, 3, and 4, indicating that their electrochemical behaviors are governed by more than one interfacial process. This means that the system cannot be described by a single charge transfer and double-layer capacitance process. Instead, passive film resistance, coating capacitance, and charge transfer resistance all contribute simultaneously. Furthermore, a phase angle moving toward $-80°$ at the intermediate-frequency region indicates strong capacitive dominance, even though multiple processes overlap. Meanwhile, in the case of the specimen #2 (Fig. 8(b)), the peak of phase angle seems to be sharper and more defined, reflecting a single interfacial time constant associated with the compact passive film forming during acidic pretreatment. For the specimen #4 (Fig. 8(d)), the shape of peaks varies for 168 h, appearing sharper within the initial hours and becoming broader over immersion time. The transition from sharp to broad peaks highlights the aging effect of immersion, where the coating initially provides strong barrier protection; over time, heterogeneity increases as the coating absorbs electrolyte and the passive film undergoes changes. For instance, the underlying passive film undergoes localized dissolution and re-precipitation at positions where electrolyte penetration and chloride ion adsorption occur, particularly at microstructural defects, grain boundaries, and coating/substrate interfaces. This phenomenon can be explained by some factors of the PANi coating structure that is not completely homogeneous caused by micro-defects and possibly due to the interaction between PANi and the initial passive layer. This creates transitional regions with mixed resistive and capacitive characteristics, altering the system frequency response. However, the phase angle remains unchanged for 168 h of immersion, demonstrating that both the passive layer and PANi coating maintain good protective properties, with capacitance dominating in charge transfer. Despite changes in electrochemical properties, the PANi coating significantly enhances corrosion resistance, especially when combined with prior surface treatment.

To further quantify the electrochemical behavior, the EIS data were fitted using an equivalent circuit model (Fig. 9(a)) and the results in Fig. 9(b–d). The circuit in Fig. 9(a) consists of R_s represents the solution resistance, CPE_1 is the constant phase element of the coating, R_{coat} is the coating resistance, CPE_2

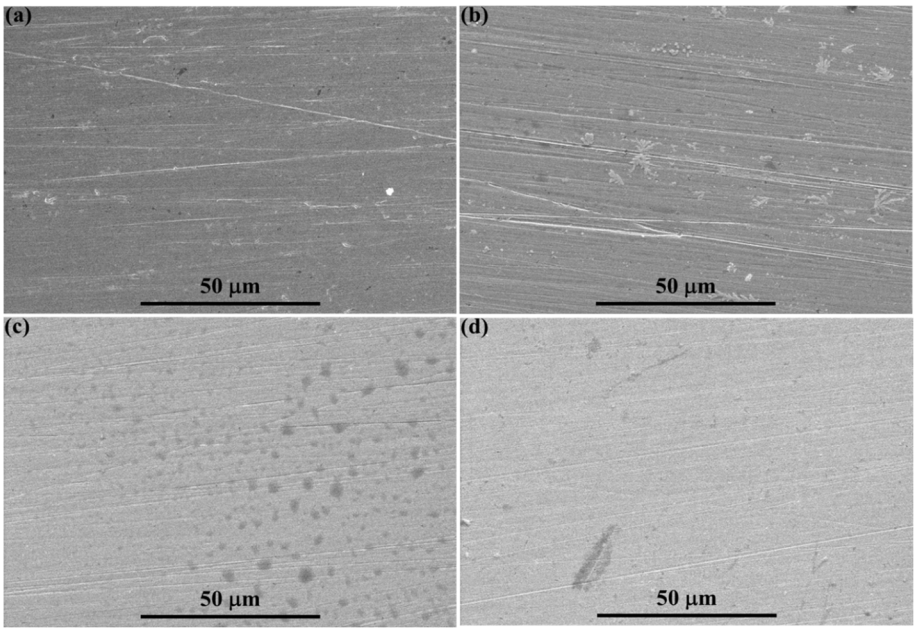

Fig. 10 Surface morphology of (a) ground 316 SS surface and (b) ground and treated 316 SS surface, and PANi coating on (c) the ground 316 SS and (d) ground and treated 316 SS after 168 h immersion in 3.5 wt% NaCl solution.

representing the non-ideal capacitance of the charge transfer process, and the charge transfer resistance R_{ct} of the substrate/coating interface. During the fitting process, the capacitance was represented by the constant phase element (CPE) to account for depressed semicircles. Among these parameters, R_{ct} is particularly important, as it reflects kinetics of the electrochemical reactions at the interface of the substrate/coating. The highest R_{ct} in Fig. 9(b) is observed for the acid-treated specimen, confirming that the compact passive film formed during pretreatment provides the most effective resistance to charge transfer and corrosion protection. When comparing with PANi coating with or without acidic treatment, R_{ct} remains lower. This trend is also consistent with R_{coat} in Fig. 9(c). This is because polyaniline allows partial electron delocalization and facilitates charge exchange across the interface and does not completely block electron transfer. In addition, the total resistance of the system (R_{total}), defined as the sum of all resistive contributions in the equivalent circuit, reflects the overall corrosion protection capability. As shown in Fig. 9(d), R_{total} increases steadily over time, with the acid treated and PANi coating sample providing the strongest overall resistance and most effective long-term protection. Overall, PANi coating after surface treatment provides great protection by improving the corrosion resistance of a 316 SS substrate in simulated seawater condition for a long immersion period.

3.3. Surface analysis after corrosion

To observe surfaces of specimens in four conditions after 168 h immersion in a 3.5 wt% NaCl solution, SEM images were employed to reveal the morphological changes, including corrosion features, coating integrity, and passive film stability (Fig. 10). Firstly, for the untreated 316 SS (#1) (Fig. 10(a)), only slight surface damage is observed, accompanied by speckled pitting distributed across the surface. This morphology suggests localized chloride ion attack at weak points in the native passive film, but the extent of damage is negligible, confirming the inherent corrosion resistance of 316 SS in the simulated seawater. This is primarily attributed to the passive film that can self-repair after minor localized dissolution, explaining why damage remains negligible even after 168 h of immersion. For the sample #2 (Fig. 10(b)), there is appearance of snowflake-like crystals that may be the product of reactions between metal ions (Fe^{2+}, Cr^{3+}, Ni^{2+}) with Cl^- or OH^- ions in the solution at nucleation sites. Although the passive layer formed after immersion in a 1 M H_2SO_4 solution has the ability to protect the surface from corrosion, it creates favorable conditions for nucleation and initiation of product crystals when 316 SS is immersed in a NaCl environment. This mean the precipitation formation process is primarily caused by the preferential adsorption of chloride ions at high-energy sites (grain boundaries, defects, and film irregularities). These sites act as heterogeneous nucleation centers for corrosion products (oxide, hydroxides, or salt deposits). In the case of the PANi-coated specimen in Fig. 10(c and d), the surface morphology of samples is insignificantly damaged, the grinding grooves as well as the appearance of crystals on the surface of the sample are no longer observed. This proves that the PANi coating was evenly applied to the entire surface, filling mechanical defects and covering uneven points, indicating that the coating process is effective, leaving no gaps or open areas. The fact that the crystals are no longer visible on the surface, partly proving that PANi created a physical or chemical barrier, limiting the formation of crystalline phases from the environment, especially the PANi coating remains durable over time when immersed in NaCl solution. On the surface of the sample #3, after 168 h of immersion in the NaCl solution, some dark spots

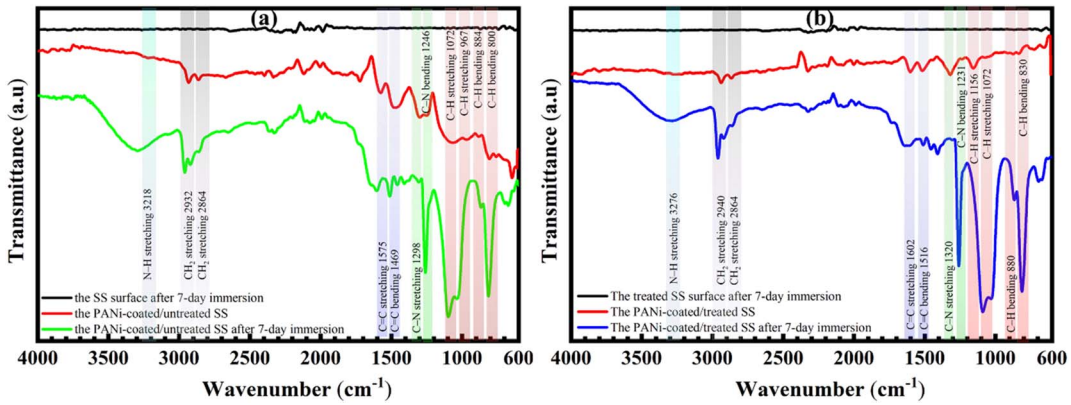

Fig. 11 Attenuated total reflectance Fourier transform infrared (ATR-FTIR) spectroscopy of (a) ground 316 SS surface and (b) ground and treated 316 SS surface specimens after 168 h-immersion in 3.5 wt% NaCl solution.

are observed, indicating localized coating degradation and the initiation of corrosion product formation beneath the polymer layer. More specifically, these spots typically correspond to localized under-film corrosion, where chloride ions penetrate through micro-defects or pores in the PANi coating. Once the passive film beneath is destabilized, corrosion products (oxide/hydroxide form) appear as darkened regions in SEM. In contrast, no such spots are observed on the sample #4 (Fig. 10(d)), indicating superior coating integrity that effectively prevents chloride ion penetration and suppresses localized under-film corrosion during 168 h of immersion. This underscores that acidic pretreatment enriched the surface with a compact passive film that may improve adhesion between PANi and the 316 SS substrate. This effect minimized micro-defects and pathways for electrolyte ingress, resulting in a more uniform and stable protective behavior during prolonged immersion.

To confirm the integrity of the PANi coating on the SS surface after immersion 168 h in the 3.5 wt% NaCl, ATR-FTIR results are shown in Fig. 11. The results obtained show that PANi coating on both the untreated and treated 316 SS maintains after 7 day immersion in the NaCl solution with clearer peaks as compared with the spectra of the original specimen. There are still characteristic peaks of PANi recorded, including N–H stretching at ~3300 cm^{-1}, C–H stretching at ~2900 cm^{-1}, C=N quinoid at ~1570 cm^{-1}, C=C benzenoid at ~1480 cm^{-1}, C–N at ~1300 cm^{-1} and C–H bending at ~1140 cm^{-1}. Additionally, a slight and minimal shift in wavenumber is observed, indicating that the PANi coating retains its fundamental chemical structure after immersion, with no significant alteration in the characteristic vibrational modes. These shifts can be attributed to minor interactions with water molecules, chloride ions, or slight changes in hydrogen bonding. Since the shifts are minimal, they do not indicate structure degradation, confirming the coating's chemical stability in the corrosive NaCl solution, correlating to electrochemical results and SEM images for 168 h immersion.

3.4. Corrosion and protection mechanism

To better understand each mechanism that takes places in four conditions: (#1) bare 316 SS (untreated substrate), (#2) treated 316 SS, (#3) PANi-coated/untreated 316 SS, and (#4) PANi-coated/treated 316 SS when immersed in the simulated seawater, each mechanism will be discuss individually.

Firstly, for the bare SS when immersed in the NaCl solution in the presence of dissolved oxygen and water, a passive layer consisting primarily of oxides or hydroxides forms on the surface, providing initial protection against uniform corrosion. In chloride-containing solutions, dissolved oxygen promotes oxidation of chromium and iron at the interface, resulting in a passive layer composed mainly of Cr_2O_3, Fe_2O_3, hydroxide species, *etc.* Additionally, water provides hydroxyl groups that stabilize the passive layer, contributing to sustain the self-healing ability of the passive film. However, when continuously immersed in chloride-containing environments, the passive film still tends to be locally broken at weak locations, such as around impurities, surface defects, *etc.* Chloride ions with small ionic radius and high diffusivity can easily penetrate through micro-defects and pores in the passive film, adsorption at high-energy sites such as grain boundaries or inclusions. The result is that the passive layer is broken at these locations; over time, forming a small pit that can be re-passivated or further developed, which is considered the initial stage in the pitting corrosion process. At the beginning of pitting corrosion initiation, the passive film begins to dissolve and release metal ions (Me^+) into the solution. These ions immediately hydrolyze with water:[49]

$$Me^{n+} + H_2O \rightarrow Me(OH)^{(n-1)} + H^+ \quad (2)$$

Therefore, the hydrolysis reaction generates H^+ ions, reducing the local pH in the pit, making the pit environment more acidic, even when the external solution is neutral or alkaline. This is a self-maintaining mechanism, with more dissolved metal generating more H^+, decreasing the pH and increasing corrosion. The pitting process can be divided into three main stages.[4] After the initial breakdown stage, the pitting reaction can be re-passivated or continue to develop steadily, in which the pits expand but do not reach a permanent state, and many sites stop growing due to re-passivation. However, a few pits have shapes and chemical conditions favorable enough to

maintain a local corrosion environment. When reaching the stable growth stage, the shape and internal conditions (low pH, high chloride concentration) maintain corrosion, causing the pores to expand rapidly in both depth and diameter, causing a serious reduction in material strength. An important note is that the destruction of the passive layer on the surface of 316 SS only occurs when the applied potential exceeds the pitting potential (E_{pit}). Before reaching this value, the passive layer remains stable; if locally broken, it has the ability to reform itself thanks to dissolved oxygen and the alloy composition rich in Cr and Mo. Under normal environmental conditions, the main mechanism of the passive layer is local destruction with continuous re-passivation, helping the surface maintain corrosion resistance. This explains why 316 SS continuously immersed in the NaCl solution for 168 h only appears slight corrosion, as shown in SEM image (Fig. 10(a)).

Secondly, for the treated SS with 1 M H_2SO_4, it is divided into two stage. At the first stage, when the sample is immersed in a 1 M H_2SO_4 solution in 1 hour, SO_4^{2-} anions are considered inhibitory anions, as they effectively adsorb onto the 316 SS surface and stabilize the passive film by suppressing localized dissolution. The reason for this is that SO_4^{2-} is a negatively charged ion with strong adsorption affinity to the oxide surface of stainless steel. When adsorbed, it forms a stable negative ion layer on the surface, covering small defects of the initial passive layer, reducing the possibility of other ions directly approaching the metal surface. Furthermore, SO_4^{2-} ions can participate in the reformation of the passive film by bonding with metal cations (Fe^{3+} and Cr^{3+}) in the oxide layer, making the passive film more durable, and less likely to be broken. During the re-passivation process on stainless steel, SO_4^{2-} ions not only adsorb onto the surface but also have the ability to bond directly with high-valent metal cations located in the oxide lattice of the film. This binding can take place in the form of a complex or a lesser sulfate salt, according to the process:[50]

$$2M^{n+} + nO^{2-} \rightarrow M_2O_n (n \in \mathbb{R}) \quad (3)$$

These ionic-electrostatic bonds or complexing ionic bonds retain the metal cations right at the membrane area, limiting their diffusion into the solution. As a result, cations (such as Fe^{3+} or Cr^{3+}) continue to participate in hydrolysis and oxidation reactions *in situ* to form hydroxide products.[50]

$$M^{n+} + nOH^- \rightarrow M(OH)_n \equiv \frac{1}{2}M_2O_n \cdot nH_2O (n \in \mathbb{R}) \quad (4)$$

This process adds and rearranges the oxide crystals, making the passive film more uniform, denser, and less defective, which involves the inward diffusion of anions from the electrolyte into the passive layer, thus contributing additional material to the oxide lattice. This mechanism leads to the formation of a double-layer passive film on the metal surface, consisting of a compact inner barrier layer and a porous outer layer. A schematic diagram of the physicochemical processes occurring within the passive film, as described in the point defect model (PDM) by Macdonald.[50] At the same time, the presence of SO_4^{2-} ions shift the potential of the electrochemical system to the positive direction, thereby making local dissolution more difficult and increasing the pitting potential of SS in the simulated seawater,[51] which has been shown in the PD analysis. Furthermore, SO_4^{2-} ions play an important role in filling in defect sites such as grain boundaries, mechanical scratches or micro-pores, where the passive film structure is less complete.[52] Therefore, in the SEM observation of the treated 316 SS surface, the scratches on the sample surface are visibly faded. Additionally, when immersed in a 3.5 wt% NaCl, the surface appears with snowflake-like precipitate (Fig. 10(b)), which is frequently related to the local corrosion process and the precipitation of poorly soluble salts. This happens because chloride ions in the solution can easily penetrate and disrupt the passive film, creating pitting corrosion spots. This film (even after being treated with H_2SO_4) is not perfect and always contains defects such as oxygen vacancies (positively charged) or cation vacancies (negatively charged). These Cl^- ions are strongly attracted to positively charged sites such as oxygen vacancies, but they must lose the surrounding water layer (hydration layer), which requires additional energy. If the electrostatic attraction is large enough to compensate, Cl^- may take up space in the defect, destabilizing the film structure. When the passive film is broken, the metals at the bottom of the pit are oxidized to M^{n+} metal ions and go into solution. Inside the pit, the hydrolysis reaction of the metal ions produces H^+, making the environment more acidic, causing some of the metal ions to diffuse out, where the pH is higher and there are anions such as OH^-. Here, they react to form precipitates and stick around the mouth of the pit to form crystals of hydroxide or metal salts. These crystals do not grow in solid blocks but develop in many branches radiating from a center, like the branched structure of a snowflake. The reason is that the crystallization process is fast, the ion concentration is high at the contact area, and the uneven distribution of reactants causes the crystals to grow in a preferential direction, creating a characteristic flared shape. This type of precipitation is both a sign of pitting corrosion and shows that the surrounding environment has reached a state of saturation and strong crystallization.

Thirdly, the untreated SS was coated with PANi before and after immersion in the NaCl solution. To understand the results obtained, it is necessary to first explain the interaction mechanism between PANi and the SS surface, emphasizing the role of PANi as a physical barrier, helping to limit the direct contact between the corrosive solution and the metal substrate. The interaction process between PANi and the SS surface can be divided into three mechanisms as mechanical, chemical and electrostatic. Mechanically, this type of interaction is based on the physical blocking phenomenon between polymer chains and microscopic irregularities (micro-pores, scratches, roughness) on the metal surface. When PANi is in a liquid state during the coating process, the polymer chains can penetrate the small channel on the steel surface, creating a mechanical connection when the coating hardens. However, when the surface is not treated, the roughness and low surface energy may lead to less uniform PANi coverage, resulting in the phenomenon of patchiness or peeling of the coating, reducing

the protective effect. Chemically, PANi can form weak bonds with hydroxyl groups or metal oxides on the SS surface. With no H_2SO_4 surface treatment, the surface of the sample retains the appearance of a natural oxide layer, where the amine (–NH–) and imine (=N–) groups in the PANi chain can create hydrogen bonds with the hydroxide groups (–OH) on the metal oxide surface. The nitrogen atoms in PANi can act as ligands, forming coordination bonds with metal ions such as Fe^{3+} or Fe^{2+} present in the oxide layer in a Lewis acid manner. In addition, Van der Waals interaction plays an important role but often be ignored in explaining the interfacial interactions of PANi to the metal surface, especially after the sample was ground and formed a nano- or micro-structured oxide layer. However, this is only an interaction force, not a covalent one, as PANi can only adhere to the SS surface through the attraction between molecules, especially when the surface is rough. Although not as strong as chemical bonds, Van der Waals forces still help the PANi layer not to peel off easily in extreme environments. After continuously immersion for 168 h, the formation of dark spots on the surface of the sample was observed at the microscopic level. This is because PANi coating is uneven and has defects when the SS surface is not treated with acid, which has been analyzed in detail in the EIS results. At defect locations, water and ions in the solution favorably penetrate, causing oxidation reactions at the surface and creating corrosion products. In another case, PANi can be deprotonated or decomposed as the long-term immersion in aggressive environments, reducing the protective ability and leading to the formation of oxidation zones. But in the case of the PANi coated/treated specimen, the appearance of round spots is no longer recorded on the sample surface, which means that the surface treatment process is not only a sub-step but also a key factor for the durability and effectiveness of the coating. Similar to the case of PANi with the ground sample surface, PANi mainly interacts with the treated sample through the oxide layer and passive sulfate salts forming on the sample as immersion in H_2SO_4. In which, the passive layer creates groups containing OH^-, SO_4^{2-}, metal oxides that can interact with amine and imine groups in the PANi chain through hydrogen bonding or electrostatic interactions. In addition, the passive layer helps improve interfacial interactions of PANi by providing a more uniform, active surface compared to the mechanically ground surface. While the mechanically ground surface has uneven roughness, creating micro-concave and convex areas that make it difficult for the coating to spread evenly, the passive layer helps to flatten and homogenize the surface at the nanoscale, thus facilitating PANi to spread and adhere evenly.

During the spin coating process, 3 ÷ 4 drops of PANi solution are continuously dripped onto the center of the sample, to create a uniform coating and evenly cover the surface of the sample. The PANi molecules bond together through a π–π stacking mechanism, not a covalent bond such as a single, double or triple bond, but a non-covalent interaction, namely a weak molecular attraction between aromatic ring systems.[53,54] It does not create a chemical bond of the shared electron type but has a great influence on the structure and properties of the material. In essence, benzene aromatic rings have π-electron systems located above and below the ring plane, so when two aromatic rings are close together, the π-electron clouds interact through London dispersion forces (a form of Van der Waals force) and quadrupole interactions (negative charge at the ring eye and positive charge at the edge, creating an attraction between oppositely charged regions). Specifically, the London dispersion force is a weak attraction between molecules that oscillate instantaneously, creating an instantaneous dipole, which is the main mechanism in π–π stacking interactions without chemical bonding. Meanwhile, the quadrupole interaction at the ring face and the positive charge at the edge, create a quadrupole moment and when the two rings are stacked off-center, the oppositely charged regions can interact and increase the attractive force, resulting in the improved pitting corrosion resistance of PANi-coated/treated 316 SS.

4. Conclusions

The work demonstrated the efficiency of acidic treatment on increasing performance of PANi coating on the 316 SS surface, characterized by both surficial observations and electrochemical measurements. The results obtained lead to the following conclusions:

1. The morphological features of SS surfaces in four conditions have a clear difference, with the coated cases exhibiting more roughness. The thickness of the PANi is estimated to be approximately 500 nm. From AFM observation, the SS surface after acidic treatment has grinding marks filled with the passive layer, resulting in a reduction of mark's depth to 0.05 μm as compared to 0.08 μm for the untreated specimen and the PANi-coated/treated specimen exhibits the highest CA of approximately 90°.

2. Electrochemical results indicate that either PANi coating or acidic treatment significantly improve pitting potential and impedance values of the electrochemical system. In which, the pitting potential is ranked in order of the untreated 316 SS < the PANi-coated/untreated 316 SS < the treated 316 SS < the PANi-coated/treated 316 SS. The results calculated show the PANi-coated/treated 316 SS surface exhibits the highest protective efficiency of ~94.7 ± 0.9% and remains consistent at the passive potential of +400 $mV_{Ag/AgCl}$, as well as highest coating, and total resistances.

3. ATR-FTIR results after 168 h immersion indicate all peaks of PANi remain unchanged, demonstrating the integrity of PANi in the 3.5 wt% NaCl solution. In particular, SEM images of specimens after 168 h immersion indicate that the PANI-coated/treated surface is clearly improved with no precipitates on the surface as compared to other cases.

Hence, the combination of acidic pretreatment and spin coating is a promising way in enhancing the pitting resistance of 316 SS, as it synergistically improves passive film stability and the interfacial properties of the coating system.

Conflicts of interest

There are no conflicts to declare.

Data availability

All data supporting this study, including ATR-FTIR spectra, contact angle, SEM, AFM, potentiodynamic polarization, potentiostatic polarization, and EIS data are contained within the main text of the article.

Supplementary information (SI) is available. See DOI: https://doi.org/10.1039/d6ra01684g.

References

1 D. Gopi, V. C. A. Prakash and L. Kavitha, Evaluation of hydroxyapatite coatings on borate passivated 316L SS in Ringer's solution, *Mater. Sci. Eng., C*, 2009, **29**(3), 955–958, DOI: 10.1016/j.msec.2008.08.020.

2 M. Talha, C. K. Behera and O. P. Sinha, In–vitro long term and electrochemical corrosion resistance of cold deformed nitrogen containing austenitic stainless steels in simulated body fluid, *Mater. Sci. Eng., C*, 2014, **40**, 455–466, DOI: 10.1016/j.msec.2014.04.006.

3 A. A. Oshkour, S. Pramanik, M. Mehrali, Y. H. Yau, F. Tarlochan and N. A. A. Osman, Mechanical and physical behavior of newly developed functionally graded materials and composites of stainless steel 316L with calcium silicate and hydroxyapatite, *J. Mech. Behav. Biomed. Mater.*, 2015, **49**, 321–331, DOI: 10.1016/j.jmbbm.2015.05.020.

4 B. Yuan, C. Yan, Z. Li, L. Li and C. Wang, Dynamic pitting processes of 316 stainless steel in NaCl + Na_2CO_3 solution with digital holography, *Corros. Commun.*, 2021, **4**, 57–67, DOI: 10.1016/j.corcom.2022.02.001.

5 F. Bartolomeu, M. Buciumeanu, E. Pinto, N. Alves, O. Carvalho, F. S. Silva and G. Miranda, 316L stainless steel mechanical and tribological behavior–A comparison between selective laser melting, hot pressing and conventional casting, *Addit. Manuf.*, 2017, **16**, 81–89, DOI: 10.1016/j.addma.2017.05.007.

6 R. F. A. Jargelius-Pettersson and B. G. Pound, Examination of the role of molybdenum in passivation of stainless steels using ac impedance spectroscopy, *J. Electrochem. Soc.*, 1998, **145**(5), 1462–1469, DOI: 10.1149/1.1838505.

7 S. Zuo-Jiang, Z. Tian, X. Jiang, H. Yu and D. Sun, Research on pitting corrosion of 316 stainless steel in the deep–sea water and sediments of the South China Sea, *Mater. Charact.*, 2025, **225**, 115176, DOI: 10.1016/j.matchar.2025.115176.

8 C. M. B. Martins, J. L. Moreira and J. I. Martins, Corrosion in water supply pipe stainless steel 304 and a supply line of helium in stainless steel 316, *Eng. Fail. Anal.*, 2014, **39**, 65–71, DOI: 10.1016/j.engfailanal.2014.01.017.

9 A. Pardo, M. C. Merino, A. E. Coy, F. Viejo, R. Arrabal and E. Matykina, Effect of Mo and Mn additions on the corrosion behaviour of AISI 304 and 316 stainless steels in H_2SO_4, *Corros. Sci.*, 2008, **50**(3), 780–794, DOI: 10.1016/j.corsci.2007.11.004.

10 F. Gao, Y. Qiao, J. Chen, L. Yang, H. Zhou, Z. Zheng and L. Zhang, Effect of nitrogen content on corrosion behavior of high–nitrogen austenitic stainless steel, *npj Mater. Degrad.*, 2023, **7**(1), 75, DOI: 10.1038/s41529–023–00394–x.

11 D. Li, F. Huang, X. Lei and Y. Jin, Localized corrosion of 304 stainless steel triggered by embedded MnS, *Corros. Sci.*, 2023, **211**, 110860, DOI: 10.1016/j.corsci.2022.110860.

12 H. Bhadeshia, R. Honeycombe, *Stainless Steel, in Steels: Microstructure and Properties*, Elsevier, 2017, 343–376, DOI: 10.1016/B978–0–08–100270–4.00012–3.

13 X. Wang, H. S. Zurob, J. D. Embury, X. Ren and I. Yakubtsov, Microstructural features controlling the deformation and recrystallization behaviour Fe–30%Mn and Fe–30%Mn–0.5%C, *Mater. Sci. Eng., A*, 2010, **527**(16–17), 3785–3791, DOI: 10.1016/j.msea.2010.03.014.

14 Z. Li, H. Luo, L. Hou, Q. Zhao, X. Wang and Y. Chang, Effect of Mn addition on the corrosion behavior of FeCrNiMn Si alloys in simulated seawater environment, *Corros. Sci.*, 2025, **252**, 112978, DOI: 10.1016/j.corsci.2025.112978.

15 J. T. Miller, H. J. Martin and E. Cudjoe, Comparison of the effects of a sulfuric acid environment on traditionally manufactured and additive manufactured stainless steel 316L alloy, *Addit. Manuf.*, 2018, **23**, 272–286, DOI: 10.1016/j.addma.2018.08.023.

16 T. Czerwiec, N. Renevier and H. Michel, Low–temperature plasma–assisted nitriding, *Surf. Coat. Technol.*, 2000, **131**(1–3), 267–277, DOI: 10.1016/S0257–8972(00)00792–1.

17 L. G. Petrova, V. A. Aleksandrov and P. E. Demin, Thermochemical treatment of steels in the plasma of a hydrostatic glow–spark discharge, *Met. Sci. Heat Treat.*, 2012, **54**(5–6), 309–314, DOI: 10.1007/s11041–012–9503–6.

18 X. Wang, T. Feng, G. Li, Y. Wang, X. Chen and K. Wang, Nanoarchitectonics with highly porous, thick, stable anodic films on 304 stainless steel for high–performance supercapacitors, *J. Phys. Chem. Solids*, 2025, **202**, 112690, DOI: 10.1016/j.jpcs.2025.112690.

19 S. Kannan, A. Balamurugan and S. Rajeswari, H_2SO_4 as a passivating medium on the localized corrosion resistance of surgical 316L SS metallic implant and its effect on hydroxyapatite coatings, *Electrochim. Acta*, 2004, **49**(15), 2395–2403, DOI: 10.1016/j.electacta.2004.01.003.

20 Y. Yue, C. Liu, P. Shi and M. Jiang, Passivity of stainless steel in sulphuric acid under chemical oxidation, *Corros. Eng. Sci. Technol.*, 2018, **53**(3), 173–182, DOI: 10.1080/1478422X.2017.1388648.

21 J. S. Noh, N. J. Laycock, W. Gao and D. B. Wells, Effects of nitric acid passivation on the pitting resistance of 316 stainless steel, *Corros. Sci.*, 2000, **42**(12), 2069–2084, DOI: 10.1016/S0010–938X(00)00052–4.

22 N. Padhy, R. Paul, U. K. Mudali and B. Raj, Morphological and compositional analysis of passive film on austenitic stainless steel in nitric acid medium, *Appl. Surf. Sci.*, 2011, **257**(11), 5088–5097, DOI: 10.1016/j.apsusc.2011.01.026.

23 Y. Li, M. B. Ives, K. S. Coley and J. R. Rodda, Corrosion of nickel–containing stainless steel in concentrated sulphuric acid, *Corros. Sci.*, 2004, **46**(8), 1969–1979, DOI: 10.1016/j.corsci.2003.10.017.

24 L. Zhang, W. Du, A. Nautiyal, Z. Liu and X. Zhang, Recent progress on nanostructured conducting polymers and composites: synthesis, application and future aspects, *Sci.*

China Mater., 2018, **61**(3), 303–352, DOI: 10.1007/s40843–017–9206–4.

25 S. O. Pehkonen and S. Yuan, *Conducting Polymer Coatings as Effective Barrier to Corrosion*, 2018, 23–61, DOI: 10.1016/B978–0–12–813584–6.00003–X.

26 M. Goyal, K. Singh and N. Bhatnagar, Conductive polymers: A multipurpose material for protecting coating, *Prog. Org. Coat.*, 2024, **187**, 108083, DOI: 10.1016/j.porgcoat.2023.108083.

27 R. Gašparac and C. R. Martin, Investigations of the mechanism of corrosion inhibition by polyaniline. polyaniline–coated stainless steel in sulfuric acid solution, *J. Electrochem. Soc.*, 2001, **148**(4), B138, DOI: 10.1149/1.1354615.

28 A. Kalendová, I. Sapurina, J. Stejskal and D. Veselý, Anticorrosion properties of polyaniline–coated pigments in organic coatings, *Corros. Sci.*, 2008, **50**(12), 3549–3560, DOI: 10.1016/j.corsci.2008.08.044.

29 E. Armelin, R. Pla, F. Liesa, X. Ramis, J. I. Iribarren and C. Alemán, Corrosion protection with polyaniline and polypyrrole as anticorrosive additives for epoxy paint, *Corros. Sci.*, 2008, **50**(3), 721–728, DOI: 10.1016/j.corsci.2007.10.006.

30 D. P. Le, Y. H. Yoo, J. G. Kim, S. M. Cho and Y. K. Son, Corrosion characteristics of polyaniline–coated 316L stainless steel in sulphuric acid containing fluoride, *Corros. Sci.*, 2009, **51**(2), 330–338, DOI: 10.1016/j.corsci.2008.10.028.

31 V. Brusic, M. Angelopoulos and T. Graham, Use of polyaniline and its derivatives in corrosion protection of copper and silver, *J. Electrochem. Soc.*, 1997, **144**(2), 436–442, DOI: 10.1149/1.1837428.

32 R. Racicot, R. Brown and S. C. Yang, Corrosion protection of aluminum alloys by double–strand polyaniline, *Synth. Met.*, 1997, **85**(1–3), 1263–1264, DOI: 10.1016/S0379–6779(97)80232–9.

33 A. J. Dominis, G. M. Spinks and G. G. Wallace, Comparison of polyaniline primers prepared with different dopants for corrosion protection of steel, *Prog. Org. Coat.*, 2003, **48**(1), 43–49, DOI: 10.1016/S0300–9440(03)00111–5.

34 N. D. Nam, J. G. Kim, Y. J. Lee and Y. K. Son, Effect of thermal treatment on the corrosion resistance of polyaniline in H_2SO_4–HF acid mixture solution, *Corros. Sci.*, 2009, **51**(12), 3007–3013, DOI: 10.1016/j.corsci.2009.08.034.

35 P. Kaushik, R. Bharti, R. Sharma, M. Verma, R. T. Olsson and A. Pandey, Progress in synthesis and applications of polyaniline-coated nanocomposites: A comprehensive review, *Eur. Polym. J.*, 2024, **221**, 113574, DOI: 10.1016/j.eurpolymj.2024.113574.

36 A. A. M. Farag, A. Ashery and M. A. Rafea, Optical dispersion and electronic transition characterizations of spin coated polyaniline thin films, *Synth. Met.*, 2010, **160**(1–2), 156–161, DOI: 10.1016/j.synthmet.2009.10.024.

37 J. A. Syed, H. Lu, S. Tang and X. Meng, Enhanced corrosion protective PANI–PAA/PEI multilayer composite coatings for 316SS by spin coating technique, *Appl. Surf. Sci.*, 2015, **325**, 160–169, DOI: 10.1016/j.apsusc.2014.11.021.

38 M. Långberg, F. Zhang, E. Grånäs, C. Örnek, J. Cheng, M. Liu, C. Wiemann, A. Gloskovskii, T. F. Keller, C. Schlueter, S. Kulkarni, H. Noei, D. Lindell, U. Kivisäkk, E. Lundgren, A. Stierle and J. Pan, Lateral variation of the native passive film on super duplex stainless steel resolved by synchrotron hard X-ray photoelectron emission microscopy, *Corros. Sci.*, 2020, **174**, 108841, DOI: 10.1016/j.corsci.2020.108841.

39 B. Jordanov, D. Tsankov and E. H. Korte, Peculiarities in the stretching vibrations of the methylene groups, *J. Mol. Struct.*, 2003, **651–653**, 101–107, DOI: 10.1016/S0022-2860(02)00632-4.

40 Z. Ping, In situ FTIR–attenuated total reflection spectroscopic investigations on the base–acid transitions of polyaniline. Base–acid transition in the emeraldine form of polyaniline, *J. Chem. Soc., Faraday Trans.*, 1996, **92**(17), 3063–3067, DOI: 10.1039/FT9969203063.

41 N. Y. Samoylova, R. N. Vasin, S. V. Sumnikov, O. Y. Ponomareva, M. E. Donets, E. A. Korneeva and E. V. Andreev, Effect of drying on the polyaniline-coated Prussian white cathode material for sodium-ion batteries, *J. Phys. Chem. Solids*, 2025, **204**, 112762, DOI: 10.1016/j.jpcs.2025.112762.

42 D. Geethalakshmi, N. Muthukumarasamy and R. Balasundaraprabhu, Structural and optical study of spin-coated camphorsulfonic acid-doped polyaniline/titanium-dioxide nanoparticles hybrid thin films, *Superlattices Microstruct.*, 2015, **82**, 447–460, DOI: 10.1016/j.spmi.2015.03.006.

43 V. Gautam, A. Srivastava, K. P. Singh and V. L. Yadav, Vibrational and gravimetric analysis of polyaniline/polysaccharide composite materials, *Polym. Sci. Ser. A*, 2016, **58**(2), 206–219, DOI: 10.1134/S0965545X16020085.

44 S. Zhu, W. Deng and Y. Su, Recent advances in preparation of metallic superhydrophobic surface by chemical etching and its applications, *Chin. J. Chem. Eng.*, 2023, **61**, 221–236, DOI: 10.1016/j.cjche.2023.02.018.

45 E. Khamme and R. Sakdanuphab, Study of corrosion properties of carbon steel, 304 and 316L stainless steels in sulfuric acid and their degradation products, *J. Met. Mater. Miner.*, 2023, **33**(4), 1672, DOI: 10.55713/jmmm.v33i4.1672.

46 A. Hickling and D. J. G. Ives, The electrochemical behaviour of iron oxides in dilute sulphuric acid and the interpretation of the flade potential of iron, *Electrochim. Acta*, 1975, **20**(1), 63–69, DOI: 10.1016/0013-4686(75)85046-8.

47 G. Giridhar, R. K. N. R. Manepalli and G. Apparao, *Contact Angle Measurement Techniques for Nanomaterials*, Elsevier, 2017, 173–195. doi: DOI: 10.1016/B978-0-323-46139-9.00008-6.

48 D. Taneichi, R. Haneda and K. Aramaki, A novel modification of an alkanethiol self-assembled monolayer with alkylisocyanates to prepare protective films against copper corrosion, *Corros. Sci.*, 2001, **43**(8), 1589–1600, DOI: 10.1016/S0010-938X(00)00152-9.

49 J. R. Galvele, Transport processes and the mechanism of pitting of metals, *J. Electrochem. Sco.*, 1976, **123**(4), 464–474, DOI: 10.1149/1.2132857.

50 D. D. Macdonald, The point defect model for the passive state, *J. Electrochem. Soc.*, 1992, **139**(12), 3434–3449, DOI: 10.1149/1.2069096.

51 G. Yang, Y. Du, S. Chen, Y. Ren and Y. Ma, Effect of secondary passivation on corrosion behavior and semiconducting properties of passive film of 2205 duplex stainless steel, *J. Mater. Res. Technol.*, 2021, **15**, 6828–6840, DOI: 10.1016/j.jmrt.2021.11.118.

52 B. Deng, Y. Jiang, J. Liao, Y. Hao, C. Zhong and J. Li, Dependence of critical pitting temperature on the concentration of sulphate ion in chloride-containing solutions, *Appl. Surf. Sci.*, 2007, **253**(18), 7369–7375, DOI: 10.1016/j.apsusc.2007.03.034.

53 S. M. Butterfield, P. R. Patel and M. L. Waters, Contribution of aromatic interactions to α-helix stability, *J. Am. Chem. Soc.*, 2002, **124**(33), 9751–9755, DOI: 10.1021/ja026668q.

54 J. H. Deng, J. Luo, Y. L. Mao, S. Lai, Y. N. Gong, D. C. Zong and T. B. Lu, π-π stacking interactions: Non-negligible forces for stabilizing porous supramolecular frameworks, *Sci. Adv.*, 2020, **6**(2), eaax9976, DOI: 10.1126/sciadv.aax9976.